Osteocyte death and bone overgrowth in mice lacking Fibroblast Growth Factor Receptors 1 and 2 in mature osteoblasts and osteocytes

Jennifer McKenzie, PhD[1,3#], Craig Smith[2#], Kannan Karuppaiah, PhD[2#], Joshua Langberg[2], Matthew J. Silva, PhD[1,3], David M. Ornitz, MD, PhD[2,3*]

Departments of [1]Orthopaedic Surgery and [2]Developmental Biology, and [3]Musculoskeletal Research Center; Washington University School of Medicine; St. Louis, Missouri, 63110; USA

[#] Authors made equal contributions to this work.

* Correspondence
David Ornitz
Department of Developmental Biology
3905 South Bldg. (campus box 8103)
Washington University School of Medicine
660 S. Euclid Avenue
St. Louis, MO 63110

Telephone: (314) 362-3908
Email: dornitz@wustl.edu

Funding

Department of Developmental Biology (DMO), NIH grants AR050211 (MJS) and HD049808 (DMO), and the Washington University Musculoskeletal Research Center (NIH P30 AR057235).

Supplemental data

This manuscript contains 2 supplemental tables and 3 supplemental figures.

Disclosures

Authors have no conflict of interest.

Abstract

Fibroblast Growth Factor (FGF) signaling pathways have well established roles in skeletal development, with essential functions in both chondrogenesis and osteogenesis. In mice, previous conditional knockout studies suggested distinct roles for FGF receptor 1 (FGFR1) signaling at different stages of osteogenesis and a role for FGFR2 in osteoblast maturation. However, the potential for redundancy among FGFRs and the mechanisms and consequences of stage-specific osteoblast lineage regulation were not addressed. Here, we conditionally inactivate *Fgfr1* and *Fgfr2* in mature osteoblasts with an Osteocalcin-Cre or Dentin matrix protein 1-CreER driver. We find that young mice lacking both receptors or only FGFR1 are phenotypically normal. However, after 6 weeks of age these *Fgfr1/Fgfr2* double- and *Fgfr1* single-conditional knockout mice develop a high bone mass phenotype with increased periosteal apposition, increased endocortical woven bone with increased porosity, and biomechanical properties that reflect increased bone mass but reduced material properties. Histopathological and gene expression analyses show that this phenotype is preceded by a striking loss of osteocytes, and gradual activation of the Wnt/βCatenin signaling pathway. These data identify a role for FGFR1 signaling in mature osteoblasts/osteocytes that is required for osteocyte survival during postnatal bone growth.

Key Words

Molecular pathways-remodeling; Osteoblasts; Osteocytes; Fibroblast Growth Factors; Apoptosis

Introduction

Osteoprogenitors in the periosteum and bone marrow give rise to matrix producing osteoblasts. As bone grows, osteoblasts can become quiescent bone lining cells, die through apoptosis, or differentiate into osteocytes, long-lived cells that become embedded within the mineralized bone matrix.[1,2] Although embedded within mineralized bone, osteocytes maintain communication with the periosteum, endosteum, and vasculature through a system of channels that form the osteocyte lacunocanalicular network.

Osteocytes function as sensory cells that respond to mechanical loading and other signals by releasing soluble factors that regulate osteoblast anabolic activity, mineral homeostasis, and osteoclast activity. In response to mechanical loading, osteocytes produce prostaglandin E2 which inhibits expression of Sclerostin, a negative regulator of anabolic Wnt signaling in osteoblasts.[3-7] Osteocytes also respond to parathyroid hormone (PTH), which likewise functions to suppress Sclerostin, accounting for some of the anabolic effects of PTH.[8] Osteocytes are a major source of the cytokine receptor activator of NF**k**B ligand (RANKL). Mechanical unloading and PTH signaling stimulate RANKL expression in osteocytes.[8-11] Osteocytes are also a major source of FGF23, an endocrine member of the Fibroblast Growth Factor (FGF) family that primarily signals to the kidney proximal tubules to suppress phosphate resorption.[12,13]

Fibroblast Growth Factor (FGF) signaling has well established roles in bone development with essential functions in both chondrogenesis and osteogenesis.[14] In humans, mutations in FGF receptors (FGFRs) 1 and 2 that affect osteogenesis are found in Crouzon, Apert, Pfeifer, and Bent bone dysplasia syndromes. These mutations result in ligand dependent activation of the mutant FGFR and, in some cases, change in the ligand binding specificity of the FGFR. The only documented example of a FGFR loss of function mutation occurs in CATSHL syndrome, in which loss of FGFR3 results in skeletal overgrowth due to increased chondrogenesis.[14,15]

FGFRs are expressed in most, if not all, skeletal lineages throughout development, and in mature bone. *Fgfr1* is expressed throughout limb bud mesenchyme at similar levels in condensing

and surrounding cells. In condensing mesenchyme that will give rise to skeletal tissue, *Fgfr2* expression increases relative to the surrounding mesenchyme.[16-21] Cells in the periphery of the mesenchymal condensation form the perichondrium and periosteum and express both *Fgfr1* and *Fgfr2*.[17,20] In the definitive periosteum of developing bone, *Fgfr1* is expressed in mesenchymal progenitors and *Fgfr2* is expressed in differentiating osteoblasts.[22-26] In the periosteum of mature bone, FGFR2 expression is lost, while FGFR1 expression persists in a subpopulation of perivascular cells, some of which express the pericyte marker NG2.[27] During fracture repair, expression of both FGFR1 and FGFR2 are increased,[28] and both FGFR1 and FGFR2 are expressed in periosteal derived mesenchymal stem cells.[27] These expression patterns suggest the potential for both unique and redundant functions of *Fgfr1* and *Fgfr2* in the osteoblast lineage.

Conditional inactivation of *Fgf* ligands and receptors in skeletal lineages has been a successful approach to identify function during development and following injury. Conditional inactivation of *Fgfr1* and *Fgfr2* in limb bud mesenchyme (using *Prx1-Cre)*, or inactivation of *Fgfr1* in all mesenchyme (using *T(brachyury)-Cre*) causes severe skeletal hypoplasia,[29,30] whereas inactivation of *Fgfr1* or *Fgfr2* in distal limb bud mesenchyme (using *AP2-Cre*) causes only a mild skeletal phenotype,[31,32] suggesting redundancy between FGFRs 1 and 2 in distal limb mesenchyme. Conditional inactivation of *Fgfr1* in osteoprogenitor cells using *Col2a1-Cre* results in increased proliferation and delayed differentiation and matrix mineralization, and conditional inactivation of *Fgfr1* in committed osteoblasts using *Col1a1-Cre* causes enhanced mineralization and cortical bone thickening in 5- to 8-month-old mice.[23] However, the mechanisms by which FGFR1 affects bone development and growth are not known. In contrast to *Fgfr1*, mice conditionally lacking *Fgfr2* in all bone lineages or harboring a mutation in the mesenchymal splice variant of *Fgfr2* (*Fgfr2c*), show impaired ossification, and decreased bone mineral density, suggesting that *Fgfr2* is a positive regulator of osteoblast maturation.[17,33] The function of FGFR2 in mature osteoblast lineages is not known.

In this study, we investigated the bone-specific function of *Fgfr1* and *Fgfr2* in mature

osteoblast/osteocyte-specific static and inducible conditional knockout mice. We find that mice lacking *Fgfr1* and *Fgfr2,* or *Fgfr1* alone, in mature osteoblasts develop a dramatic high bone mass phenotype that becomes histologically evident between 6 and 12 weeks of age. Bone pathology initiates as early as 3 weeks of age with the onset of osteocyte loss, which progresses to nearly complete loss by 12 weeks. This phenotype is recapitulated with a postnatal conditional knockout model that progresses with a similar time course. Biomechanical studies show that although whole-bone strength is increased in correlation with increased mass, bone material properties are diminished. These studies show that FGFR1 signaling in mature osteoblasts is essential for osteocyte viability and that the absence of FGFR1, either directly or secondary to osteocyte loss, increases bone formation.

Materials and Methods

Mice

Mice were housed in a pathogen-free facility and handled in accordance with standard use protocols, animal welfare regulations, and the NIH Guide for the Care and Use of Laboratory Animals. All protocols were approved by the Washington University Animal Studies Committee.

Fgfr1$^{f/f}$,[34] *Fgfr2*$^{f/f}$,[33] *OC-Cre*,[35] *Dmp1-CreER*,[36] *ROSA*^{Tomato} (Ai9 allele),[37] *ROSA*^{mTmG},[38] mice have been previously described. All mice for these studies are maintained on a mixed C57BL/6; 129X1 genetic background. Homozygous floxed alleles of *Fgfr1* and *Fgfr2* were maintained as double floxed mice (DFF) and outbred to hybrid C57BL/6J;129X1 mice every second generation and then backcrossed to homozygosity. *OC-Cre; Fgfr1*$^{f/f}$*; Fgfr2*$^{f/f}$ mice are maintained by crossing *OC-Cre; Fgfr1*$^{f/f}$*; Fgfr2*$^{f/f}$ males to *Fgfr1*$^{f/f}$*; Fgfr2*$^{f/f}$ females, resulting in a 50% yield of experimental and *Fgfr1*$^{f/f}$*; Fgfr2*$^{f/f}$ (DFF) mice (which serve as one type of control). A similar mating scheme was used to generate *Dmp1-CreER*; *Fgfr1*$^{f/f}$*; Fgfr2*$^{f/f}$ mice. To induce Cre activation in *Dmp1-CreER; Fgfr1*$^{f/f}$*; Fgfr2*$^{f/f}$ and *Fgfr1*$^{f/f}$*; Fgfr2*$^{f/f}$ control mice, tamoxifen chow (400mg/kg, Envigo Teklad, TD.130860) was given from 3 to 5 weeks of age.

MicroCT and DXA Imaging

In vivo microCT was done on the right tibia and femur to evaluate cortical and cancellous bone measures over time (VivaCT 40, Scanco Medical, Wayne, PA; X-ray tube potential 70 kV, integration time 300 ms, X-ray intensity 114 μA, isotropic voxel size 21 μm, frame averaging 1, projections 1024, medium resolution scan). Measurements were made according to recommended standards,[39] with cortical bone measured for 1 mm (48 slices) at a location 5 mm proximal to the tibia fibula junction: total area (T.Ar), bone area (B.Ar), cortical thickness (Ct.Th), tissue mineral density (TMD), and polar moment of inertia (pMOI). Metaphyseal bone was analyzed from a region 600 μm (28 slices) distal to the proximal growth plate in the tibia and proximal to the distal growth plate in the femur. Because of the blurred distinction between the cortical shell and the adjacent cancellous bone in the DCKO mice at ages > 12 weeks, we analyzed all tissue inside the periosteal margin (cortical shell + cancellous bone). Outcomes were: total volume (TV), bone volume (BV), bone volume to total volume ratio (BV/TV), and volumetric bone mineral density (vBMD). *In vivo* dual energy X-ray absorptiometry (UltraFocus100 DXA module, Faxitron, Tuscon, Arizona) was used to measure percent fat, bone mineral content (BMC) and areal bone mineral density (aBMD) for the whole body of the mouse (excluding the head). To evaluate growth, body weight was recorded prior to each scan. Mice were scanned at 6, 12, 18, 24 and 32 weeks of age. For the *Dmp1-CreER*; *Fgfr1*$^{f/f}$; *Fgfr2*$^{f/f}$ mice the bones were scanned *ex vivo* (X-ray tube potential 55 kV, integration time 300 ms, X-ray intensity 145 μA, isotropic voxel size 10 μm, frame averaging 1, projections 2048, high resolution scan), embedded in 2% agarose.

Dynamic Histomorphometry

To mark bone formation, 12-week-old mice were injected with calcein green (10 mg/kg, IP, Sigma) and 5 days later with alizarin red (25 mg/kg, IP, Sigma), which was given 2 days prior to euthanasia. Tibia were embedded in poly-methyl methacrylate (plastic) and 100 μm thick cross-sections of the diaphysis were cut 5 mm proximal to the tibiofibular junction. Sections were mounted to glass slides and polished to a thickness of approximately 30 μm. To visualize the

calcein and alizarin labels fluorescent images were taken (Olympus IX51 with Olympus DP70 camera or Leica TCS SPE Confocal). Following published standards[40], the bone sections were analyzed for mineral apposition rate (MAR), mineralizing surface per bone surface (MS/BS) and bone formation rate per bone surface (BFR/BS) on the endocortical (Ec) and periosteal (Ps) surfaces (BIOQUANT OSTEO, BIOQUANT Image Analysis Corporation, Nashville, TN).

Biomechanics

At 24 weeks age the mechanical properties of the femurs were evaluated with mechanical testing. Prior to testing, the midshaft of these bones (100 slices, 2.1 mm) were imaged with microCT to determine bone morphology (VivaCT 40, Scanco Medical, same parameters as above). After scanning, the femurs were prepared for three-point bending (span = 7 mm). Bones were preloaded to -0.3 N, then a displacement ramp of 0.1 mm/s was applied until failure (Dynamight 8841, Instron, Norwood, MA). As recommended by Jepsen et al.,[41] the structural mechanical properties acquired from bending tests were stiffness, yield load, maximum load, post-yield displacement, and work-to-fracture. In combination with the bone morphology (moment of inertia) and beam theory, the estimated material properties of Young's modulus, yield stress, and maximum stress were calculated. After whole-bone testing was completed, reference point indentation (RPI) testing was done at four locations near the midshaft (two on each side of the break). The parameters measured included first indentation distance (ID 1st), total indentation distance (TID), indentation distance increase (IDI), first unloading slope (US 1st), and average creep indentation distance (CID).

Histology, immunohistochemistry, and immunofluorescence

For histological analysis of long bones, intact femurs and tibias were isolated, fixed in 4% PFA/PBS overnight at 4°C or fixed in 10% buffered formalin overnight at room temperature. Bones were rinsed in water several times and decalcified in 14% EDTA/PBS for 2 weeks. Paraffin-embedded tissue sections (5 μm) were stained with Hematoxylin and Eosin (H&E), tartrate resistant acid phosphatase (TRAP), von Kossa or Alizarin Red.

For immunohistochemistry, paraffin sections or cryosections were rehydrated and treated with 0.3% hydrogen peroxide in methanol for 15 min to suppress endogenous peroxidase activity. Antigen retrieval was achieved by microwaving the sections in 10 mM citrate buffer (pH 6.0) for 10 min followed by gradual cooling to room temperature. Sections were incubated overnight at 4°C with the following primary antibodies: DMP1 (Abcam, ab82351; 1:100), mSOST (RD systems, AF1589; 1:100). Secondary antibody was Alexa Fluor 488 donkey anti-rabbit (Life Technologies, A21206; 1:1000). Immunofluorescence imaging was performed on a Zeiss Apotome II fluorescence microscope.

TUNEL staining was performed using the DeadEnd Flurometric TUNEL system staining kit (Promega, G3250). All kit instructions were followed for paraffin-embedded tissues with a 5 min proteinase K treatment and fixation with 4% paraformaldehyde. Negative controls with rTdT Enzyme were run with each group. Imaging was performed on a Leica TCS SPE Confocal microscope.

Determination of osteocyte density and viability

Osteocytes were histologically categorized as alive, dying, and dead based on their appearance on H&E stained cortical sections (see Figure 5J below). Alive cells were characterized by a whole nucleus with little to no empty space in the lacuna. Dying cells were identified morphologically as having either a fragmented nucleus or a small polarized nucleus within an otherwise empty lacuna. Dead cells were identified as having little or no hematoxylin-stained material in an otherwise empty lacuna. A small number of histological features (<10%) could not be assigned a definitive category and were not counted. These may represent histological sectioning artifacts or ossified lacunae. Osteocytes from all three categories were counted in the anterior tibial cortex in a 3 mm region beginning 1 mm from the growth plate. Osteocyte density was calculated by dividing the number of counted cells/lacunae by the area of cortical bone. Cortical bone area was quantified by measuring the total bone area in the analysis region and then subtracting the area of any region inside this total bone area that was not cortical

bone, e.g. marrow space or other cavities.

Real-time quantitative PCR (RT-qPCR)

We used quantitative RT-PCR (qPCR) to examine the expression of marker genes in total RNA isolated from flushed cortical bone from 3 and 12-week-old *Fgfr1*$^{f/f}$*; Fgfr2*$^{f/f}$ and *OC-Cre; Fgfr1*$^{f/f}$*; Fgfr2*$^{f/f}$ mice. Mid-diaphyseal cortical bone was dissected, the marrow was flushed immediately, and the bone tissues were individually frozen in liquid nitrogen and stored at −80°C until analysis. Frozen tissues were pulverized in a dry ice-cooled stainless-steel flask with a ball bearing in a Micro Dismembrator (Sartorius) at 2000 rpm for 20 s. RNA was stabilized with Trizol Reagent (#10296– 010, Life Technologies Corporation, USA) and total RNA isolation was prepared according to the manufacturer's instructions. cDNA was synthesized using the iScript Select cDNA Synthesis Kit (#1708841, Bio-Rad). mRNA expression was measured using TaqMan Fast Advanced Master Mix (#4444557, Life Technologies) and TaqMan assay probes for *Alp, Axin2, Col1a1, Dmp1, Fgfr1, Fgfr2, Fgf23, Lef1, Lrp5,* and *Sost. Hprt* was used as a normalization control.

Sample size and statistics

Based on the coefficient of variation from previous microCT data and a goal to detect a difference in cortical area of 30% (CV=18%), group sample sizes (n) of n=6 mice were chosen. For quantitative analysis of cell number, cell death, proliferation, or level of gene expression our goal was to detect a 20% difference between control and experimental samples; a sample size of n=4-6 mice were chosen based on average CV (~20%) from recent data. Two-factor ANOVA for DXA, microCT, and histological (osteocyte) measurements; time and genotype were independent factors. Mechanical testing, dynamic histomorphometry, and gene expression measures were evaluated with unpaired t-tests between genotypes groups. All statistical analyses were performed using commercial software (GraphPad Prism 7, La Jolla, CA). Data are represented as mean ± standard deviation (SD). Statistical significance was considered at $p < 0.05$. In all cases, sample size (n) represents the number of animals per group, which includes approximately

equal numbers of males and females.

Results

Increased bone formation in mice lacking Fgfr1 and Fgfr2 in mature osteoblasts

To investigate the role of FGFR1 and FGFR2 signaling in mature osteoblasts and osteocytes, *Fgfr1*$^{f/f}$*; Fgfr2*$^{f/f}$ (*Fgfr1/2* DFF) mice were crossed with mice carrying the *Osteocalcin-Cre* (*OC-Cre*) transgenic allele to generate *Fgfr1*; *Fgfr2* double conditional knockouts (OC-*Fgfr1/2* DCKO).[33-35] The OC-Cre transgene becomes active beginning at ~E17,[35] and targets the mature osteoblast lineage (endosteum, periosteum and osteocytes). Activity is not detected in non-skeletal tissues.[35] The activity of *OC-Cre* was confirmed by generating *OC-Cre, ROSA*^{Tomato} (Ai9 allele) and *OC-Cre, ROSA*^{mTmG} mice. Cre-dependent reporter expression was only observed in the endosteum, periosteum, and osteocytes (Supplemental Figure 1A). Quantitative RT-PCR analysis of mRNA made from flushed cortical bone showed significantly decreased expression of *Fgfr1* and *Fgfr2* in OC-*Fgfr1/2* DCKO mice compared to *Fgfr1/2* DFF controls, confirming efficient deletion (Supplemental Figure 1B).

Fgfr1/2 DFF control mice and OC-*Fgfr1/2* DCKO mice are healthy and fertile and appeared phenotypically normal. Body weight of all mice in the study increased over time, with no differences between OC-*Fgfr1/2* DCKO and *Fgfr1/2* DFF mice at any timepoint (Figure 1A). *In vivo* DXA imaging showed that the percent body fat remained consistent from 6 to 24 weeks and was not affected by genotype (Figure 1B). However, DXA imaging revealed that whole body bone mineral content (BMC) and areal bone mineral density (aBMD) were both greater in OC-*Fgfr1/2* DCKO mice compared to controls, becoming statistically significant at 18 weeks-of-age (Figure 1C-D). By 24 weeks of age, BMC was 80% higher and aBMD was 30% higher in OC-*Fgfr1/2* DCKO mice, with no apparent difference between male and female mice.

To quantitatively assess changes in bone structure over time, control and OC-*Fgfr1/2* DCKO mice were monitored by *in vivo* microCT between 6 and 32 weeks of age. Compared to controls,

OC-*Fgfr1/2* DCKO mice revealed a progressive accrual of cortical and cancellous bone occurring after 6 weeks of age in both male and female mice (Figure 1E-H). In the diaphysis of the bone there were no significant differences in cortical area at 6 weeks of age, but by 12 weeks DCKO mice had 107% greater cortical area (Fig 1E-F). Furthermore, total area and pMOI were increased compared to age matched controls in mice 12 weeks and older (Supplemental Table S1). From 18-32 weeks of age there were dramatic increases in total area, cortical area, pMOI, and cortical thickness. Lower cortical TMD (~8% reduction) was observed in 12-week-old OC-*Fgfr1/2* DCKO mice compared to *Fgfr1/2* DFF controls. Similar changes were observed in the femur (not shown). Overall, the shape of the long bones appeared normal over this time course.

Consistent with changes in diaphyseal cortical bone, the tibia metaphyseal compartment also showed greater TV, BV, BV/TV and vBMD in DCKO mice vs. controls; these differences became significant starting at 18 weeks of age and remained elevated through 32 weeks of age (Figure 1G-H, Supplemental Table S1). By 32 weeks of age, BV was 180% greater in OC-*Fgfr1/2* DCKO mice. The results were similar for the metaphyseal region in the distal femur (Supplemental Table S1).

To assess the relative contributions of *Fgfr1* and *Fgfr2* to the regulation of bone growth, we generated *OC-Cre; Fgfr1*$^{f/f}$*; Fgfr2*$^{f/+}$ and *OC-Cre; Fgfr1*$^{f/+}$*; Fgfr2*$^{f/f}$ single conditional knockout (CKO) mice that are heterozygous for a floxed allele of the other *Fgfr*. Analysis of these mice at 6, 12 and 18 weeks of age by *in vivo* microCT showed that the increased bone mass phenotype in OC-*Fgfr1/2* DCKO mice can be accounted for by inactivation of *Fgfr1* alone (Supplemental Figure 2). Furthermore, *OC-Cre; Fgfr1*$^{f/+}$*; Fgfr2*$^{f/f}$ mice also serve as controls for OC-Cre, showing that the *OC-Cre* allele does not contribute to any of the noted bone phenotypes and that one wild type allele of *Fgfr1* is sufficient for normal bone growth.

Increased whole-bone strength but reduced material properties in* OC-*Fgfr1/2* DCKO *bone

The increased bone mass in OC-*Fgfr1/2* DCKO mice suggested that their bones would have

increased strength at the whole bone (structural) level. The whole-bone mechanical properties and material properties of femurs from 24-week-old mice were assessed by three-point bending and reference point indentation (RPI). Three-point bending analysis revealed several significant differences in structural mechanical properties of OC-*Fgfr1/2* DCKO mice. Compared to controls, OC-*Fgfr1/2* DCKO mice showed an 88% increase in yield load, 82% increase in maximum load, and 46% increase in stiffness, but a 71% decrease in post-yield displacement (Figure 2A-D, Supplemental Table S2). Work-to-fracture was unaffected by genotype, due the offsetting effects of increased maximum load and decreased post-yield displacement. MicroCT imaging of the femur midshaft showed increased total area and bone area, and an apparent increased porosity in OC-*Fgfr1/2* DCKO mice compared to *Fgfr1/2* DFF control mice (Figure 2E). These features resulted in a 5-fold increase in polar moment of inertia (pMOI) (Figure 2H). Estimated material properties, including Young's modulus, yield stress, and maximum stress, were significantly less by 70%, 44%, and 45%, respectively, in DCKO versus controls (Figure 2F, G, Supplemental Table S2). Reference Point Indentation (RPI) testing demonstrated no significant differences in ID 1st, TID, IDI, US 1st or CID parameters between OC-*Fgfr1/2* DCKO and *Fgfr1/2* DFF mice (Supplemental Table S2).

Increased mineralized bone and increased osteoblast and osteoclast activity in OC-FGFR1/2* DCKO *mice

Histological analysis of 12-week-old mice is consistent with the microCT data, showing increased cancellous and cortical bone in OC-*Fgfr1/2* DCKO mice compared to *Fgfr1/2* DFF control mice (Figure 3A). In contrast, the growth plate showed histologically normal proliferating and hypertrophic chondrocytes (Figure 3B). Cortical bone histology of OC-*Fgfr1/2* DCKO mice shows relatively normal appearing lamellar bone on the periosteal side but an increase in woven bone on the endocortical side (Figure 3A). Mineralization, assessed by Von Kossa staining, showed complete mineralization of all cortical and cancellous regions (Figure 3C).

Dynamic histomorphometry of 12-week-old mice indicated increased anabolic activity in OC-

Fgfr1/2 DCKO mice compared to *Fgfr1/2* DFF control mice (Figure 4A-J). OC-*Fgfr1/2* DCKO mice had a significant increase in endocortical mineral apposition rate (MAR) (61%) and bone formation rate (BFR/BS) (55%), with no changes in mineralizing surface (MS/BS). On the periosteal surface, MAR, MS/BS and BFR/BS were all significantly increased by 35-164%. In addition, abundant double label is visible within the cortical bone of the OC-*Fgfr1/2* DCKO, which is not present in the *Fgfr1/2* DFF mouse.

Both the histology and dynamic histomorphometry indicate an increase in the porosity of the cortical bone in OC-*Fgfr1/2* DCKO mice, primarily in the endocortical woven bone region (Figure 4B, D, L, N). TRAP staining, used to identify osteoclasts, shows that cortical porosities in OC-*Fgfr1/2* DCKO mice are lined with osteoclasts, indicating active cortical remodeling (Figure 4K-N).

Osteocyte loss precedes increased bone accrual

A striking histological feature of OC-*Fgfr1/2* DCKO bone histology is the absence of nuclei within osteocyte lacunae, observed in both cortical (Figure 5) and trabecular regions (not shown). Osteocyte lacunae were histologically scored as alive, dying, or dead, based on lacunar morphology (Figure 5J). At 3 weeks of age, OC-*Fgfr1/2* DCKO cortical bone showed normal lamellar histology (Figure 5A, B). However, quantitation of nucleated lacunae (classified as alive cells) showed a 36% decrease in OC-*Fgfr1/2* DCKO tibia compared to *Fgfr1/2* DFF control tibia ($p<0.01$) and a corresponding increase in dying/dead osteocytes (Figure 5A-C). At 6 weeks of age cortical histology also showed normal appearing lamellar bone; however, there was a 64% decrease in alive osteocytes ($p<0.001$) and a corresponding increase in dying/dead osteocytes (Figure 5D-F). TRAP staining of 3-week-old OC-*Fgfr1/2* DCKO mice did not reveal qualitative differences in the abundance or appearance of osteoclasts (not shown).

Twelve-week-old mice showed a layer of normal-appearing lamellar bone on the periosteal side, and a large increase in endocortical woven bone. In both histological domains there was a dramatic absence of alive osteocytes (94% reduction, $p<0.001$) in OC-*Fgfr1/2* DCKO mice

compared to *Fgfr1/2* DFF controls and a large (54 fold) increase in the number of dead osteocyte lacunae (Figure 5G-I). The fragmented appearing osteocyte nuclei suggested apoptosis, which was confirmed by TUNEL assay, which showed abundant staining in OC-*Fgfr1/2* DCKO cortical bone, but not in *Fgfr1/2* DFF control bone (Figure 5M, N). At all three ages examined, the overall density of osteocyte lacunae remained similar in *Fgfr1/2* DFF and OC-*Fgfr1/2* DCKO mice (Figure 5K). Both genotypes showed a moderate (22-24%, $p<0.05$) decrease in lacunar density between 3 and 12 weeks-of-age. Interestingly, at 3 weeks of age, the average density of alive osteocytes in OC-*Fgfr1/2* DCKO mice was similar to that of controls at all time points (Figure 5L). This suggests that the density of living osteocytes may be the limiting factor for normal cortical bone growth.

Increased bone formation correlates with activation of Wnt/βCatenin signaling

Gene expression was analyzed in cortical bone in 3- and 12-week-old mice by quantitative RT-PCR (Figure 6). At 3 weeks of age, markers of bone formation, *Col1a1* and *Alp*, were decreased in OC-*Fgfr1/2* DCKO mice compared to *Fgfr1/2* DFF control mice, suggesting that an initial consequence of loss of FGFR1 and FGFR2 was decreased bone formation. This is consistent with reduced Wnt/βCatenin signaling, shown by lower levels of *Axin2*, *Lrp5,* and *Lef1*. Consistent with the initiation of osteocyte loss, levels of *Dmp1* and *Sost* were decreased, but paradoxically, levels of *Fgf23* were increased. At this stage, clearly the decreased level of *Sost* does not correlate with reduced Wnt/βCatenin signaling and increased level of *Fgf23* does not correlate with osteocyte loss. At 12 weeks of age, when robust woven bone formation was observed in OC-*Fgfr1/2* DCKO mice, markers of bone formation, *Col1a1* and *Alp*, were increased. Consistent with loss of most osteocytes and concurrent increased bone formation, *Sost* expression was decreased and markers of Wnt/βCatenin signaling, *Lrp5,* and *Lef1,* were increased in OC-*Fgfr1/2* DCKO mice compared to *Fgfr1/2* DFF control mice. Similar to 3-week-old OC-*Fgfr1/2* DCKO mice, levels of *Fgf23* remained high in 12-week-old mice, despite the decreased number of live osteocytes. Finally, immunostaining also showed fewer SOST and DMP1 positive cells within

cortical bone of OC-*Fgfr1/2* DCKO mice (Supplemental Figure 3).

FGFR requirements for osteocyte survival in mature mice

The phenotype caused by inactivation of *Fgfr1* and *Fgfr2* with *OC-Cre* may be due to altered development in the late embryonic or neonatal period, and/or to altered FGFR1/2 signaling in later postnatal osteoblasts and osteocytes. To distinguish between these possibilities, we used the *Dmp1-CreER* allele to initiate the inactivation of *Fgfr1* and *Fgfr2* beginning in 3-week-old mice. To compare cell populations targeted by *Dmp1-CreER* and *OC-Cre*, lineage reporters were used. Lineage analysis of *Dmp1-CreER; ROSA26*^{Tomato} (Ai9 allele) mice, induced with tamoxifen beginning at 3 weeks of age for 2 weeks, is very similar to that of adult OC-Cre, *ROSA26*^{Tomato} mice, with expression in both osteoblasts and osteocytes (compare Figure 7A, B and Supplemental Figure 1).

Dmp1-CreER; Fgfr1$^{f/f}$*; Fgfr2*$^{f/f}$ (DMP-*Fgfr1/2* DCKO) mice and *Fgfr1/2* DFF control mice were given tamoxifen chow beginning at 3 weeks of age for 2 weeks to inactivate *Fgfr1* and *Fgfr2* in osteoblasts and osteocytes. Mice were then aged to 16 weeks and limbs were examined by microCT followed by histology (Figure 7C). MicroCT analysis of 16-week-old DMP-*Fgfr1/2* DCKO mice showed increased bone area and total area in the mid tibia (Figure 7D) and mid femur (not shown). Histological analysis showed increased cortical bone accompanied by osteocyte lacunae that were empty or contained fragmented nuclei (Figure 7F-I). Similar to the OC-*Fgfr1/2* DCKO mice, DMP-*Fgfr1/2* DCKO mice showed positive TUNEL staining throughout cortical bone (Figure 7J-K).

Discussion

In this report we identify a novel function of FGFR signaling in mature osteoblasts and osteocytes which is required to maintain osteocyte viability. Inactivation of *Fgfr1* and *Fgfr2* or only *Fgfr1* in late embryonic stages with the *OC-Cre* allele resulted in osteocyte loss beginning as early as 3 weeks of age. Inactivation of *Fgfr1* and *Fgfr2* beginning at 3 weeks of age using the

tamoxifen-inducible *Dmp1-CreER* allele also led to osteocyte loss, observed at 12 (data not shown) and 16 weeks of age. Because both of these Cre alleles target mature osteoblasts and osteocytes, it is possible that FGFR signaling directly within osteocytes and/or that FGFR signaling in immediate osteocyte precursors or mature osteoblasts is required for osteocyte survival.

Osteocytes are a source of Sclerostin, a Wnt inhibitory protein product of the *Sost* gene. Reduced expression of *Sost* would be expected to lead to increased Wnt/βCatenin signaling and stimulation of osteoblast anabolic activity.[42] However, in 3-week-old OC-*Fgfr1/2* DCKO mice, *Sost* expression was reduced while Wnt/βCatenin signaling, as assessed by expression of Wnt reporter genes, showed no evidence of activation and in fact was reduced. In contrast, by 12 weeks of age, when most osteocytes were lost, *Sost* was also reduced and, as expected, some markers of Wnt/βCatenin signaling (*Lrp5*, *Lef1*) were upregulated. We posit that increased Wnt/βCatenin signaling beginning between 6 and 12 weeks of age is one factor that contributes to the observed increase in bone formation observed in 12-week and older mice.

The mechanism(s) by which loss of FGFR signaling results in osteocyte loss is not known and could involve regulation of direct cell survival pathways, regulation of the osteocyte lacunocanalicular network or the surrounding extracellular matrix, or other signaling systems in bone that affect osteocyte survival. Regulation of the lacunocanalicular network is particularly attractive given that through its transduction of mechanical force the lacunocanalicular network is important for osteocyte survival.[11,43] Additionally, osteocyte apoptosis is stimulated by estrogen withdrawal, glucocorticoids, unloading, and microdamage[11,44,45] Although the mechanisms by which these events lead to osteocyte apoptosis are poorly understood, our results raise the possibility that altered FGFR signaling may play a role. Examination of mechanisms by which FGFR signaling promotes osteocyte survival will be the subject of future studies.

The increase in bone mass in OC-*Fgfr1/2* DCKO is preceded by the initial loss of osteocytes, suggesting that increased bone accrual is secondary to osteocyte loss. This possibility could be

tested by pharmacologically inhibiting osteocyte apoptosis with the pan-caspase inhibitor QVD, which has been shown to block osteocyte apoptosis and prevent pathological bone remodeling.[11,46-48]

At both 3 and 12 weeks of age, we observed increased *Fgf23* mRNA expression in cortical bone. Given that the number of viable osteocytes is in decline, this suggests that the increased *Fgf23* expression likely occurs in osteoblasts or pre-osteocytes.[49] Interestingly, it has been shown that viable osteocytes, within 100 to 300 μm from dying osteocytes, have increased expression of VEGF and RANKL.[45,50] We posit that *Fgf23* expression may be similarly increased in nearby viable osteocytes or pre-osteocytes in response to their dying neighbors. The mechanisms leading to increased *Fgf23* in OC-*Fgfr1/2* DCKO mice are not known and likely to be indirect since available data suggests that FGFR1 signaling functions to directly promote *Fgf23* expression in osteocytes and bone marrow stromal cells.[51-53] Furthermore, genetic inactivation of *Fgfr1* in osteocytes of Hyp mice, a mouse model of X-linked hypophosphatemia (XLH), reduced the excessive FGF23 levels in osteocytes and partially rescued the bone phenotype in these mice.[54] In contrast, pharmacological activation of FGFR1 in osteoblasts led to increased FGF23 secretion and hypophosphatemia in adult mice.[55] These data support an important role for FGF23/FGFR1 signaling in the control of bone mass and mineralization *in vivo*, but through a mechanism that is distinct from that in OC-*Fgfr1/2* DCKO mice lacking FGFR1 in mature osteoblasts and osteocytes.

The FGF ligands that function in neonatal and juvenile growing bone are not known. FGF2, FGF9, and FGF18 are good candidates since FGF9 and FGF18 have established roles in bone development,[26,56-63] and FGF2 has established roles in growing and mature bone.[64] However, loss of FGF2 leads to osteoporosis, suggesting that it functions at a different stage of the osteoblast lineage, or functions through a different FGFR, such as FGFR3, which is also expressed in mature osteoblasts.[65] Future experiments will be required to determine if there is redundancy between FGF2 and FGF9/18, or unique stage-specific activities of these ligands

during osteoblast maturation in growing bone.

In conclusion, these studies establish a role for FGFR signaling in the mature osteoblast lineage in growing bone in neonatal and juvenile mice. Loss of FGFR signaling in mature osteoblasts or osteocytes either directly or indirectly leads to osteocyte death, which in turn leads to increased cortical remodeling and eventual bone mass accrual. Future studies will be required to determine whether FGFR signaling has a homeostatic role in mature bone.

Acknowledgements

The authors thank D. Leib and C. Idleburg and the Washington University Musculoskeletal Research Center for help with MicroCT and histology, and A. Robling and P. Divieti Pajevic for providing *Dmp1-CreER* mice.

Authors' Roles: Study design: JM, KK, MS and DO. Study conduct: JM, KK and CS. Data collection: JM, KK, CS and JL. Data interpretation: JM, CS, KK, MS and DO. Drafting manuscript: JM and DO. Revising manuscript: JM, CS, KK, MS and DO. Approving final version of manuscript: JM, MS and DO. JM, CS, MS, and DO take responsibility for the integrity of the data analysis.

References

1. Manolagas SC. Birth and death of bone cells: basic regulatory mechanisms and implications for the pathogenesis and treatment of osteoporosis. Endocr Rev. Apr 2000;21(2):115-37. Epub 2000/04/27.
2. Dallas SL, Prideaux M, Bonewald LF. The osteocyte: an endocrine cell ... and more. Endocr Rev. Oct 2013;34(5):658-90. Epub 2013/04/25.
3. Compton JT, Lee FY. A review of osteocyte function and the emerging importance of sclerostin. J Bone Joint Surg Am. Oct 1 2014;96(19):1659-68. Epub 2014/10/03.
4. Bonewald LF. The Role of the Osteocyte in Bone and Nonbone Disease. Endocrinol Metab Clin North Am. Mar 2017;46(1):1-18. Epub 2017/01/31.
5. Kitase Y, Barragan L, Qing H, Kondoh S, Jiang JX, Johnson ML, et al. Mechanical induction of PGE2 in osteocytes blocks glucocorticoid-induced apoptosis through both the beta-catenin and PKA pathways. J Bone Miner Res. Dec 2010;25(12):2657-68. Epub 2010/06/26.

6. Winkler DG, Sutherland MK, Geoghegan JC, Yu C, Hayes T, Skonier JE, et al. Osteocyte control of bone formation via sclerostin, a novel BMP antagonist. Embo j. Dec 1 2003;22(23):6267-76. Epub 2003/11/25.
7. van Bezooijen RL, Roelen BA, Visser A, van der Wee-Pals L, de Wilt E, Karperien M, et al. Sclerostin is an osteocyte-expressed negative regulator of bone formation, but not a classical BMP antagonist. J Exp Med. Mar 15 2004;199(6):805-14. Epub 2004/03/17.
8. O'Brien CA, Plotkin LI, Galli C, Goellner JJ, Gortazar AR, Allen MR, et al. Control of bone mass and remodeling by PTH receptor signaling in osteocytes. PLoS One. 2008;3(8):e2942. Epub 2008/08/14.
9. Xiong J, O'Brien CA. Osteocyte RANKL: new insights into the control of bone remodeling. J Bone Miner Res. Mar 2012;27(3):499-505. Epub 2012/02/23.
10. Ben-awadh AN, Delgado-Calle J, Tu X, Kuhlenschmidt K, Allen MR, Plotkin LI, et al. Parathyroid hormone receptor signaling induces bone resorption in the adult skeleton by directly regulating the RANKL gene in osteocytes. Endocrinology. Aug 2014;155(8):2797-809. Epub 2014/06/01.
11. Cabahug-Zuckerman P, Frikha-Benayed D, Majeska RJ, Tuthill A, Yakar S, Judex S, et al. Osteocyte Apoptosis Caused by Hindlimb Unloading is Required to Trigger Osteocyte RANKL Production and Subsequent Resorption of Cortical and Trabecular Bone in Mice Femurs. J Bone Miner Res. Jul 2016;31(7):1356-65. Epub 2016/02/08.
12. Bonewald LF, Wacker MJ. FGF23 production by osteocytes. Pediatr Nephrol. Apr 2013;28(4):563-8. Epub 2012/09/18.
13. Quarles LD. Skeletal secretion of FGF-23 regulates phosphate and vitamin D metabolism. Nat Rev Endocrinol. May 2012;8(5):276-86. Epub 2012/01/18.
14. Ornitz DM, Marie PJ. Fibroblast growth factor signaling in skeletal development and disease. Genes Dev. Jul 15 2015;29(14):1463-86.
15. Ornitz DM, Legeai-Mallet L. Achondroplasia: Development, pathogenesis, and therapy. Dev Dyn. Apr 2017;246(4):291-309.
16. Sheeba CJ, Andrade RP, Duprez D, Palmeirim I. Comprehensive analysis of fibroblast growth factor receptor expression patterns during chick forelimb development. Int J Dev Biol. 2010;54(10):1517-26. Epub 2011/02/09.
17. Eswarakumar VP, Monsonego-Ornan E, Pines M, Antonopoulou I, Morriss-Kay GM, Lonai P. The IIIc alternative of Fgfr2 is a positive regulator of bone formation. Development. Aug 2002;129(16):3783-93.
18. Orr-Urtreger A, Givol D, Yayon A, Yarden Y, Lonai P. Developmental expression of two murine fibroblast growth factor receptors, flg and bek. Development. Dec 1991;113(4):1419-34. Epub 1991/12/01.
19. Peters KG, Werner S, Chen G, Williams LT. Two FGF receptor genes are differentially expressed in epithelial and mesenchymal tissues during limb formation and organogenesis in the mouse. Development. Jan 1992;114(1):233-43.
20. Delezoide AL, Benoist-Lasselin C, Legeai-Mallet L, Le Merrer M, Munnich A, Vekemans M, et al. Spatio-temporal expression of FGFR 1, 2 and 3 genes during human embryo-fetal ossification. Mech Dev. Sep 1998;77(1):19-30. Epub 1998/10/24.

21. Szebenyi G, Savage MP, Olwin BB, Fallon JF. Changes in the expression of fibroblast growth factor receptors mark distinct stages of chondrogenesis in vitro and during chick limb skeletal patterning. Dev Dyn. Dec 1995;204(4):446-56.
22. Coutu DL, Francois M, Galipeau J. Inhibition of cellular senescence by developmentally regulated FGF receptors in mesenchymal stem cells. Blood. Jun 23 2011;117(25):6801-12. Epub 2011/04/30.
23. Jacob AL, Smith C, Partanen J, Ornitz DM. Fibroblast growth factor receptor 1 signaling in the osteo-chondrogenic cell lineage regulates sequential steps of osteoblast maturation. Dev Biol. Aug 15 2006;296(2):315-28.
24. Molteni A, Modrowski D, Hott M, Marie PJ. Differential expression of fibroblast growth factor receptor-1, -2, and -3 and syndecan-1, -2, and -4 in neonatal rat mandibular condyle and calvaria during osteogenic differentiation in vitro. Bone. Apr 1999;24(4):337-47.
25. Britto JA, Evans RD, Hayward RD, Jones BM. From genotype to phenotype: the differential expression of FGF, FGFR, and TGFbeta genes characterizes human cranioskeletal development and reflects clinical presentation in FGFR syndromes. Plast Reconstr Surg. Dec 2001;108(7):2026-39; discussion 40-6.
26. Ohbayashi N, Shibayama M, Kurotaki Y, Imanishi M, Fujimori T, Itoh N, et al. FGF18 is required for normal cell proliferation and differentiation during osteogenesis and chondrogenesis. Genes Dev. Apr 1 2002;16(7):870-9.
27. Colnot C. Skeletal cell fate decisions within periosteum and bone marrow during bone regeneration. J Bone Miner Res. Feb 2009;24(2):274-82. Epub 2008/10/14.
28. Schmid GJ, Kobayashi C, Sandell LJ, Ornitz DM. Fibroblast growth factor expression during skeletal fracture healing in mice. Dev Dyn. Mar 2009;238(3):766-74.
29. Yu K, Ornitz DM. FGF signaling regulates mesenchymal differentiation and skeletal patterning along the limb bud proximodistal axis. Development. Feb 2008;135(3):483-91.
30. Verheyden JM, Lewandoski M, Deng C, Harfe BD, Sun X. Conditional inactivation of Fgfr1 in mouse defines its role in limb bud establishment, outgrowth and digit patterning. Development. Oct 2005;132(19):4235-45.
31. Li C, Xu X, Nelson DK, Williams T, Kuehn MR, Deng CX. FGFR1 function at the earliest stages of mouse limb development plays an indispensable role in subsequent autopod morphogenesis. Development. Nov 2005;132(21):4755-64.
32. Coumoul X, Shukla V, Li C, Wang RH, Deng CX. Conditional knockdown of Fgfr2 in mice using Cre-LoxP induced RNA interference. Nucleic Acids Res. 2005;33(11):e102.
33. Yu K, Xu J, Liu Z, Sosic D, Shao J, Olson EN, et al. Conditional inactivation of FGF receptor 2 reveals an essential role for FGF signaling in the regulation of osteoblast function and bone growth. Development. Jul 2003;130(13):3063-74.
34. Trokovic R, Trokovic N, Hernesniemi S, Pirvola U, Vogt Weisenhorn DM, Rossant J, et al. FGFR1 is independently required in both developing mid- and hindbrain for sustained response to isthmic signals. Embo J. Apr 15 2003;22(8):1811-23.
35. Zhang M, Xuan S, Bouxsein ML, von Stechow D, Akeno N, Faugere MC, et al. Osteoblast-specific knockout of the insulin-like growth factor (IGF) receptor gene reveals an

essential role of IGF signaling in bone matrix mineralization. J Biol Chem. Nov 15 2002;277(46):44005-12. Epub 2002/09/07.
36. Powell WF, Jr., Barry KJ, Tulum I, Kobayashi T, Harris SE, Bringhurst FR, et al. Targeted ablation of the PTH/PTHrP receptor in osteocytes impairs bone structure and homeostatic calcemic responses. J Endocrinol. Apr 2011;209(1):21-32. Epub 2011/01/12.
37. Madisen L, Zwingman TA, Sunkin SM, Oh SW, Zariwala HA, Gu H, et al. A robust and high-throughput Cre reporting and characterization system for the whole mouse brain. Nat Neurosci. Jan 2010;13(1):133-40. Epub 2009/12/22.
38. Muzumdar MD, Tasic B, Miyamichi K, Li L, Luo L. A global double-fluorescent Cre reporter mouse. Genesis. Research Support, N.I.H., Extramural Sep 2007;45(9):593-605. Epub 2007/09/18.
39. Bouxsein ML, Boyd SK, Christiansen BA, Guldberg RE, Jepsen KJ, Muller R. Guidelines for assessment of bone microstructure in rodents using micro-computed tomography. J Bone Miner Res. Jul 2010;25(7):1468-86. Epub 2010/06/10.
40. Dempster DW, Compston JE, Drezner MK, Glorieux FH, Kanis JA, Malluche H, et al. Standardized nomenclature, symbols, and units for bone histomorphometry: a 2012 update of the report of the ASBMR Histomorphometry Nomenclature Committee. J Bone Miner Res. Jan 2013;28(1):2-17. Epub 2012/12/01.
41. Jepsen KJ, Silva MJ, Vashishth D, Guo XE, van der Meulen MC. Establishing biomechanical mechanisms in mouse models: practical guidelines for systematically evaluating phenotypic changes in the diaphyses of long bones. J Bone Miner Res. Jun 2015;30(6):951-66. Epub 2015/04/29.
42. Burgers TA, Williams BO. Regulation of Wnt/beta-catenin signaling within and from osteocytes. Bone. Jun 2013;54(2):244-9. Epub 2013/03/09.
43. Noble BS, Peet N, Stevens HY, Brabbs A, Mosley JR, Reilly GC, et al. Mechanical loading: biphasic osteocyte survival and targeting of osteoclasts for bone destruction in rat cortical bone. Am J Physiol Cell Physiol. Apr 2003;284(4):C934-43. Epub 2002/12/13.
44. Brennan MA, Haugh MG, O'Brien FJ, McNamara LM. Estrogen withdrawal from osteoblasts and osteocytes causes increased mineralization and apoptosis. Horm Metab Res. Jul 2014;46(8):537-45. Epub 2014/01/22.
45. Jilka RL, Noble B, Weinstein RS. Osteocyte apoptosis. Bone. Jun 2013;54(2):264-71. Epub 2012/12/15.
46. Emerton KB, Hu B, Woo AA, Sinofsky A, Hernandez C, Majeska RJ, et al. Osteocyte apoptosis and control of bone resorption following ovariectomy in mice. Bone. Mar 2010;46(3):577-83. Epub 2009/11/21.
47. Kennedy OD, Laudier DM, Majeska RJ, Sun HB, Schaffler MB. Osteocyte apoptosis is required for production of osteoclastogenic signals following bone fatigue in vivo. Bone. Jul 2014;64:132-7. Epub 2014/04/09.
48. Kennedy OD, Lendhey M, Mauer P, Philip A, Basta-Pljakic J, Schaffler MB. Microdamage induced by in vivo Reference Point Indentation in mice is repaired by osteocyte-apoptosis mediated remodeling. Bone. Feb 2017;95:192-8. Epub 2016/12/07.
49. Martin A, David V, Quarles LD. Regulation and function of the FGF23/klotho endocrine pathways. Physiol Rev. Jan 2012;92(1):131-55. Epub 2012/02/03.

50. Kennedy OD, Herman BC, Laudier DM, Majeska RJ, Sun HB, Schaffler MB. Activation of resorption in fatigue-loaded bone involves both apoptosis and active pro-osteoclastogenic signaling by distinct osteocyte populations. Bone. May 2012;50(5):1115-22. Epub 2012/02/22.
51. Martin A, Liu S, David V, Li H, Karydis A, Feng JQ, et al. Bone proteins PHEX and DMP1 regulate fibroblastic growth factor Fgf23 expression in osteocytes through a common pathway involving FGF receptor (FGFR) signaling. FASEB J. Apr 20 2011. Epub 2011/04/22.
52. Wohrle S, Henninger C, Bonny O, Thuery A, Beluch N, Hynes NE, et al. Pharmacological inhibition of fibroblast growth factor (FGF) receptor signaling ameliorates FGF23-mediated hypophosphatemic rickets. J Bone Miner Res. Apr 2013;28(4):899-911. Epub 2012/11/07.
53. Hassan A, Durlacher K, Silver J, Naveh-Many T, Levi R. The fibroblast growth factor receptor mediates the increased FGF23 expression in acute and chronic uremia. Am J Physiol Renal Physiol. Feb 1 2016;310(3):F217-21. Epub 2015/08/28.
54. Xiao Z, Huang J, Cao L, Liang Y, Han X, Quarles LD. Osteocyte-specific deletion of Fgfr1 suppresses FGF23. PLoS One. 2014;9(8):e104154. Epub 2014/08/05.
55. Wu AL, Feng B, Chen MZ, Kolumam G, Zavala-Solorio J, Wyatt SK, et al. Antibody-Mediated Activation of FGFR1 Induces FGF23 Production and Hypophosphatemia. PLoS One. 2013;8(2):e57322. Epub 2013/03/02.
56. Hung IH, Yu K, Lavine KJ, Ornitz DM. FGF9 regulates early hypertrophic chondrocyte differentiation and skeletal vascularization in the developing stylopod. Dev Biol. Jul 15 2007;307(2):300-13.
57. Hung IH, Schoenwolf GC, Lewandoski M, Ornitz DM. A combined series of Fgf9 and Fgf18 mutant alleles identifies unique and redundant roles in skeletal development. Dev Biol. Mar 1 2016;411(1):72-84. Epub 2016/01/23.
58. Liu Z, Lavine KJ, Hung IH, Ornitz DM. FGF18 is required for early chondrocyte proliferation, hypertrophy and vascular invasion of the growth plate. Dev Biol. Feb 1 2007;302(1):80-91.
59. Liu Z, Xu J, Colvin JS, Ornitz DM. Coordination of chondrogenesis and osteogenesis by fibroblast growth factor 18. Genes Dev. Apr 1 2002;16(7):859-69.
60. Rodriguez-Zabala M, Aza-Carmona M, Rivera-Pedroza CI, Belinchon A, Guerrero-Zapata I, Barraza-Garcia J, et al. FGF9 mutation causes craniosynostosis along with multiple synostoses. Hum Mutat. Jul 21 2017. Epub 2017/07/22.
61. Tang L, Wu X, Zhang H, Lu S, Wu M, Shen C, et al. A point mutation in Fgf9 impedes joint interzone formation leading to multiple synostoses syndrome. Hum Mol Genet. Apr 01 2017;26(7):1280-93. Epub 2017/02/09.
62. Wang L, Roth T, Abbott M, Ho L, Wattanachanya L, Nissenson RA. Osteoblast-derived FGF9 regulates skeletal homeostasis. Bone. Feb 08 2017. Epub 2017/02/13.
63. Harada M, Murakami H, Okawa A, Okimoto N, Hiraoka S, Nakahara T, et al. FGF9 monomer/dimer equilibrium regulates extracellular matrix affinity and tissue diffusion. Nat Genet. 2009;41(3):289-98.

64. Coffin JD, Homer-Bouthiette C, Hurley MM. Fibroblast Growth Factor 2 and Its Receptors in Bone Biology and Disease. Journal of the Endocrine Society. Jul 1 2018;2(7):657-71. Epub 2018/06/27.
65. Xiao L, Naganawa T, Obugunde E, Gronowicz G, Ornitz DM, Coffin JD, et al. Stat1 controls postnatal bone formation by regulating fibroblast growth factor signaling in osteoblasts. J Biol Chem. Jun 25 2004;279(26):27743-52. Epub 2004/04/10.

Figure Legends

Figure 1. Increased bone mass in mice lacking FGFR1/2 in mature osteoblasts and osteocytes. (A) Body weight measurements showing no effect of genotype between 6 and 24 weeks of age. (B-D) Analysis of whole body (minus head) bone density and body fat content of OC-*Fgfr1/2* DCKO mice compared to *Fgfr1/2* DFF controls (age 6-24 weeks, n=6) using dual-energy X-ray absorptiometry (DXA). (B) Measurement of body fat content showing no effect of genotype between 6 and 24 weeks of age. (C, D) Measurement of bone mineral content (BMC) and areal bone mineral density (aBMD) showing a significant increase in OC-*Fgfr1/2* DCKO mice by 18 weeks of age. (E-H) Analysis of diaphyseal (cortical) and metaphyseal (cortical + cancellous) bone by *in vivo* microCT. MicroCT images of mid tibial (E) and proximal tibial (G) sections of *Fgfr1/2* DFF mice and OC-*Fgfr1/2* DCKO mice. (F) Quantitation of cortical area from mid tibial sections. (H) Quantitation of metaphyseal bone volume/total volume ratio (BV/TV) from proximal tibial sections.

Statistics, 2-way ANOVA with Bonferroni's multiple comparison test. ns, not significant; Pink data points, female mice; Blue data points, male mice.

Figure 2. Biomechanical properties of the femurs of OC-*Fgfr1/2* DCKO and *Fgfr1/2* DFF mice. (A) Femurs from 24-week-old mice were subjected to three-point bending to obtain a force-displacement curve. (B-D) Analysis of these data showing significant differences in maximum load (B), stiffness (C) and post yield displacement (D). (E) MicroCT imaging of the mid-femur showing increased cortical area and porosity in OC-*Fgfr1/2* DCKO compared to *Fgfr1/2* DFF mice. Analysis of material properties showing a significant decrease in Young's modulus (F), and maximum stress (G) in OC-*Fgfr1/2* DCKO compared to *Fgfr1/2* DFF mice. (H) Calculation of the polar moment of inertia showing a significant increase in OC-*Fgfr1/2* DCKO compared to

Fgfr1/2 DFF mice. Statistics, unpaired t-test. Pink data points, female mice; Blue data points, male mice.

Figure 3. Histological analysis of OC-*Fgfr1/2* DCKO and *Fgfr1/2* DFF mice. (A) H&E stained sections of the proximal tibia showing increased cortical bone in OC-*Fgfr1/2* DCKO compared to *Fgfr1/2* DFF mice at 12 weeks of age. (B) higher magnification view of the growth plate showing normal cytoarchitecture in OC-*Fgfr1/2* DCKO and *Fgfr1/2* DFF mice. (C) Von Kossa stained sections of the proximal tibia showing increased mineralized bone area in OC-*Fgfr1/2* DCKO compared to *Fgfr1/2* DFF mice. ct-lam, cortical lamellar; ct-wov, cortical woven

Figure 4. Increased bone growth and remodeling in mice lacking FGFR1/2 in mature osteoblasts and osteocytes. (A-J) Calcein and alizarin labeled transverse sections from the tibial diaphysis of *Fgfr1/2* DFF (A), OC-*Fgfr1/2* DCKO (B) mice at 12 weeks of age. (C, D) shows magnified views for the boxed regions in A and B, respectively. Image analysis of endocortical bone shows an increased mineral apposition rate (E) and bone formation rate/bone surface ratio (G), but no difference in the mineralizing surface/bone surface ratio (F) in OC-*Fgfr1/2* DCKO compared to *Fgfr1/2* DFF mice. Image analysis of periosteal bone shows an increased mineral apposition rate (H), mineralizing surface/bone surface ratio (I), and bone formation rate/bone surface ratio (J) in OC-*Fgfr1/2* DCKO compared to *Fgfr1/2* DFF mice. (K-N) TRAP staining shows increased numbers of osteoclasts in cortical bone in OC-*Fgfr1/2* DCKO (L, N) compared to *Fgfr1/2* DFF (K, M) mice. ct-lam, cortical lamellar; ct-wov, cortical woven; bm, bone marrow; p, periosteum; ns, not significant. Statistics unpaired t-test. Pink data points, female mice; Blue data points, male mice.

Figure 5. Osteocyte loss in mice lacking FGFR1/2 in mature osteoblasts and osteocytes. (A-L) Analysis of osteocyte lacunae morphology at 3, 6, and 12 weeks of age. Osteocytes were categorized according to the morphologies shown in panel J. Three-week-old mice (A-C) showing decreased numbers of "alive" osteocytes and increased numbers of "dead" and "dying" osteocytes. These differences were progressively increased at 6 weeks of age (D-F) and 12 weeks of age (G-I). (K) Analysis of lacunar density showing no effect of genotype at any age. (L) Analysis of "alive" osteocyte density showing no difference at 3 weeks of age, but reduced density at 6 and 12 weeks of age. (M, L) TUNEL staining showing increased osteocyte apoptosis in cortical bone from 12-week-old OC-*Fgfr1/2* DCKO compared to *Fgfr1/2* DFF mice. ct-lam, cortical lamellar; ct-wov, cortical woven; bm, bone marrow; p, periosteum. Statistics Alive, dying, dead, cells, OC density, 2-way ANOVA with Sidak's multiple comparison test. Lacunae density, 2-way ANOVA with Tukey's multiple comparison test.

Figure 6. Gene expression in cortical bone from OC-*Fgfr1/2* DCKO and *Fgfr1/2* DFF mice. Cortical bone (femur and tibia) from 3- and 12-week-old mice were flushed to remove bone marrow and used to prepare total RNA. Quantitative RT-PCR was used to examine changes in gene expression of osteoblast anabolic bone genes (*Col1a1, ALP*), genes preferentially expressed in osteocytes (*Dmp1, Fgf23, Sost*), and indicators of Wnt/β-catenin signaling activity (*Axin2, Lrp5, Lef1*). Statistics unpaired t-test.

Figure 7. Localization of the *Dmp1-CreER* lineage and inactivation of *Fgfr1* and *Fgfr2* in mature osteoblasts and osteocytes in postnatal mice. (A, B) Fluorescence imaging for Tomato (red) in cortical bone from *ROSA26*^{Tomato} mice (A) and *Dmp1-CreER; ROSA26*^{Tomato} mice (B) that were induced with tamoxifen chow from 3-5 weeks of age and analyzed at 6 weeks of age. (C) Experimental timeline for conditional knockout of *Fgfr1* and *Fgfr2* in postnatal mature osteoblasts and osteocytes. (D) MicroCT imaging of the mid-tibia in 16-week-old mice showing

increased cortical area and porosity in tamoxifen induced Dmp1-*Fgfr1/2* DCKO compared to *Fgfr1/2* DFF control mice. (E) Quantitation of cortical bone area and total area. (F-I) Histology (H&E stain) showing osteocyte lacunae morphology in tamoxifen-induced Dmp1-*Fgfr1/2* DCKO and *Fgfr1/2* DFF control mice at 16 weeks of age. Low magnifcation images (F, G) and high magnification images (H, I) are shown. (J, K) TUNEL staining showing increased osteocyte apoptosis in cortical bone from 16-week-old Dmp1-*Fgfr1/2* DCKO compared to *Fgfr1/2* DFF control mice that were induced with tamoxifen from 3-5 weeks of age. bm, bone marrow; ct, cortical bone; mu, muscle. Statistics unpaired t-test, ** $p < 0.01$. Pink data points, female mice; Blue data points, male mice.

Figure 1

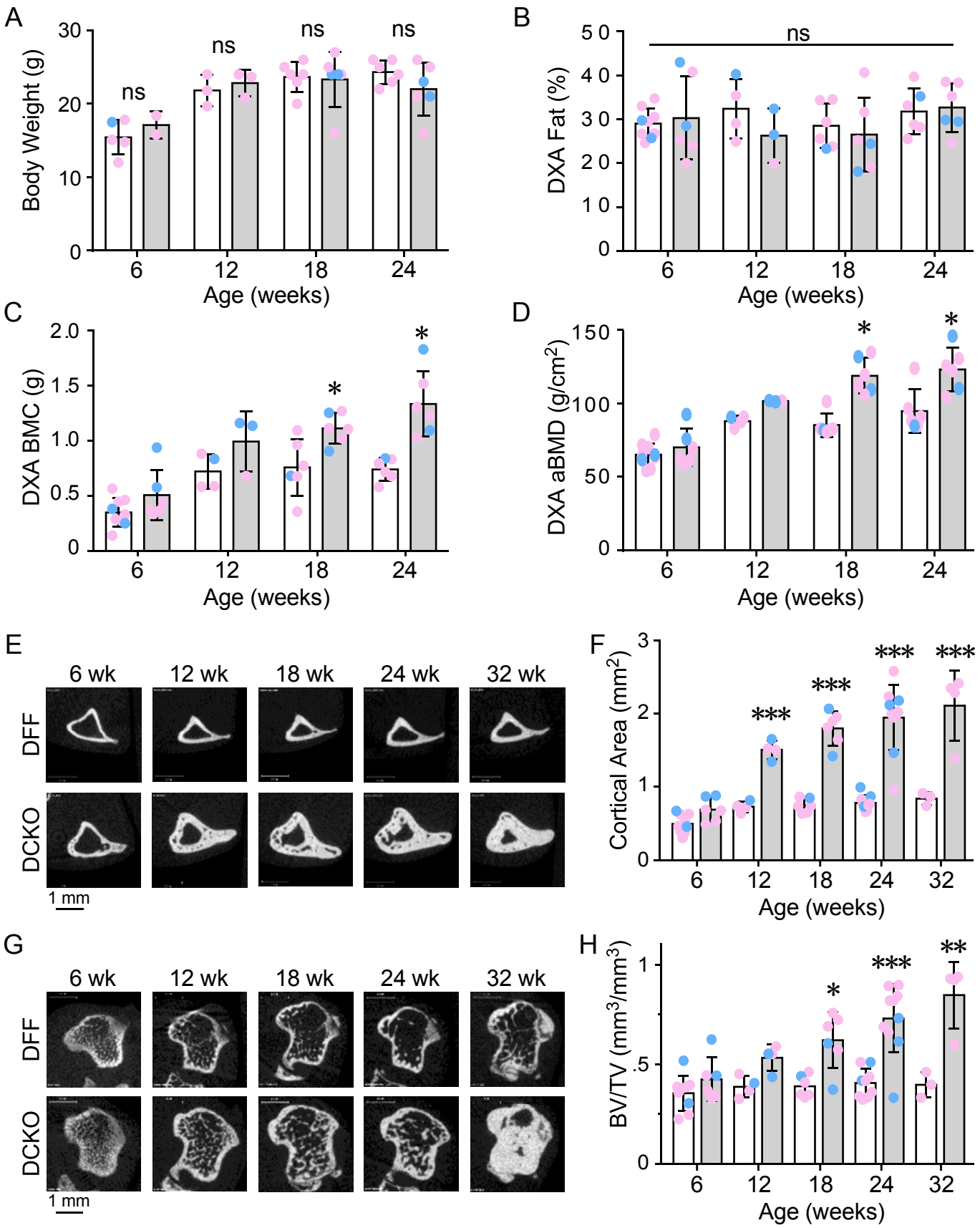

□ *Fgfr1*$^{f/f}$; *Fgfr2*$^{f/f}$ (DFF) ■ *OC-Cre; Fgfr1*$^{f/f}$; *Fgfr2*$^{f/f}$ (DCKO) * p<0.01 ** p<0.001 *** p<0.0001

Figure 2

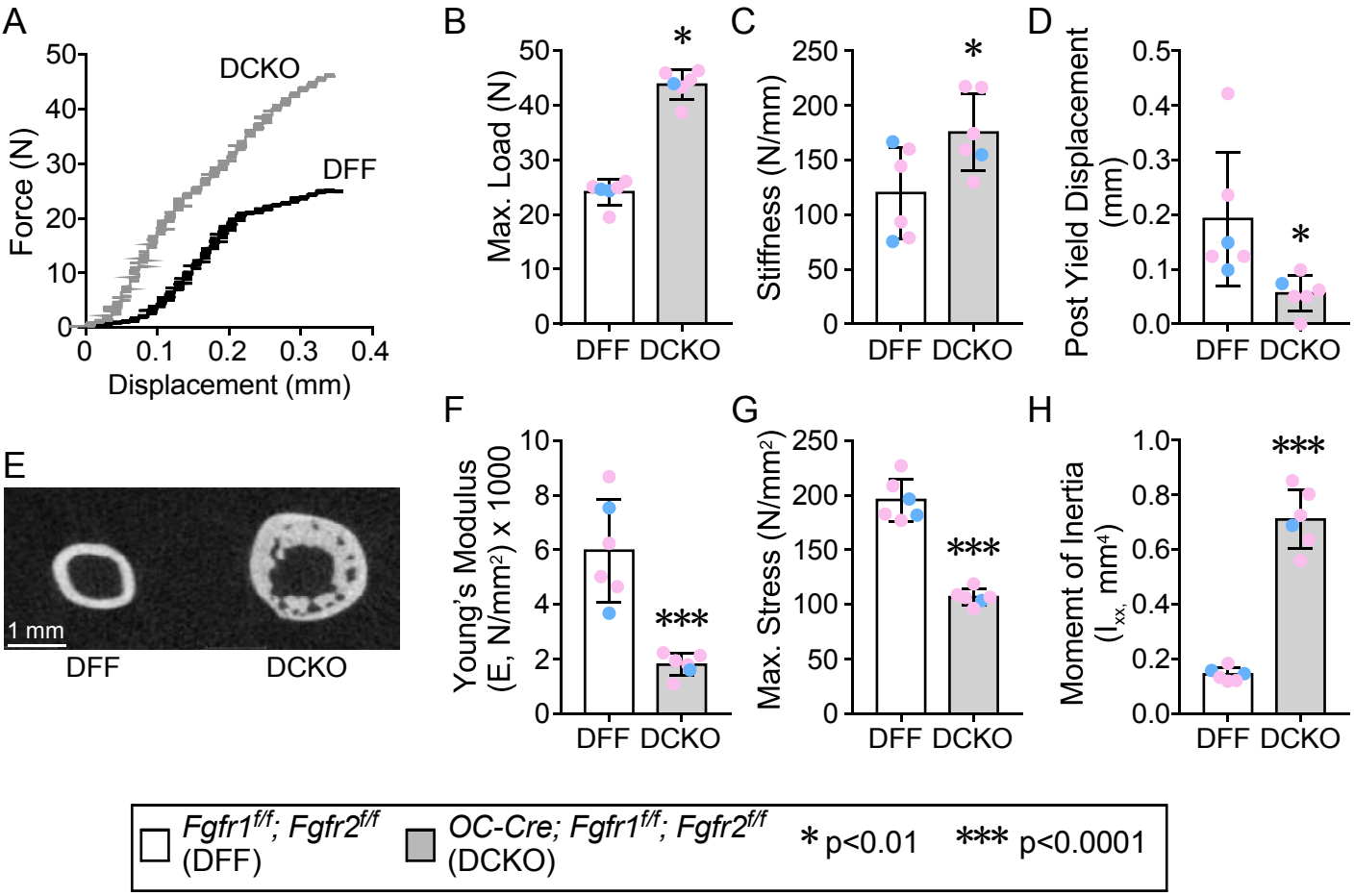

□ *Fgfr1*$^{f/f}$; *Fgfr2*$^{f/f}$ (DFF) ■ *OC-Cre; Fgfr1*$^{f/f}$; *Fgfr2*$^{f/f}$ (DCKO) * $p<0.01$ *** $p<0.0001$

Figure 3

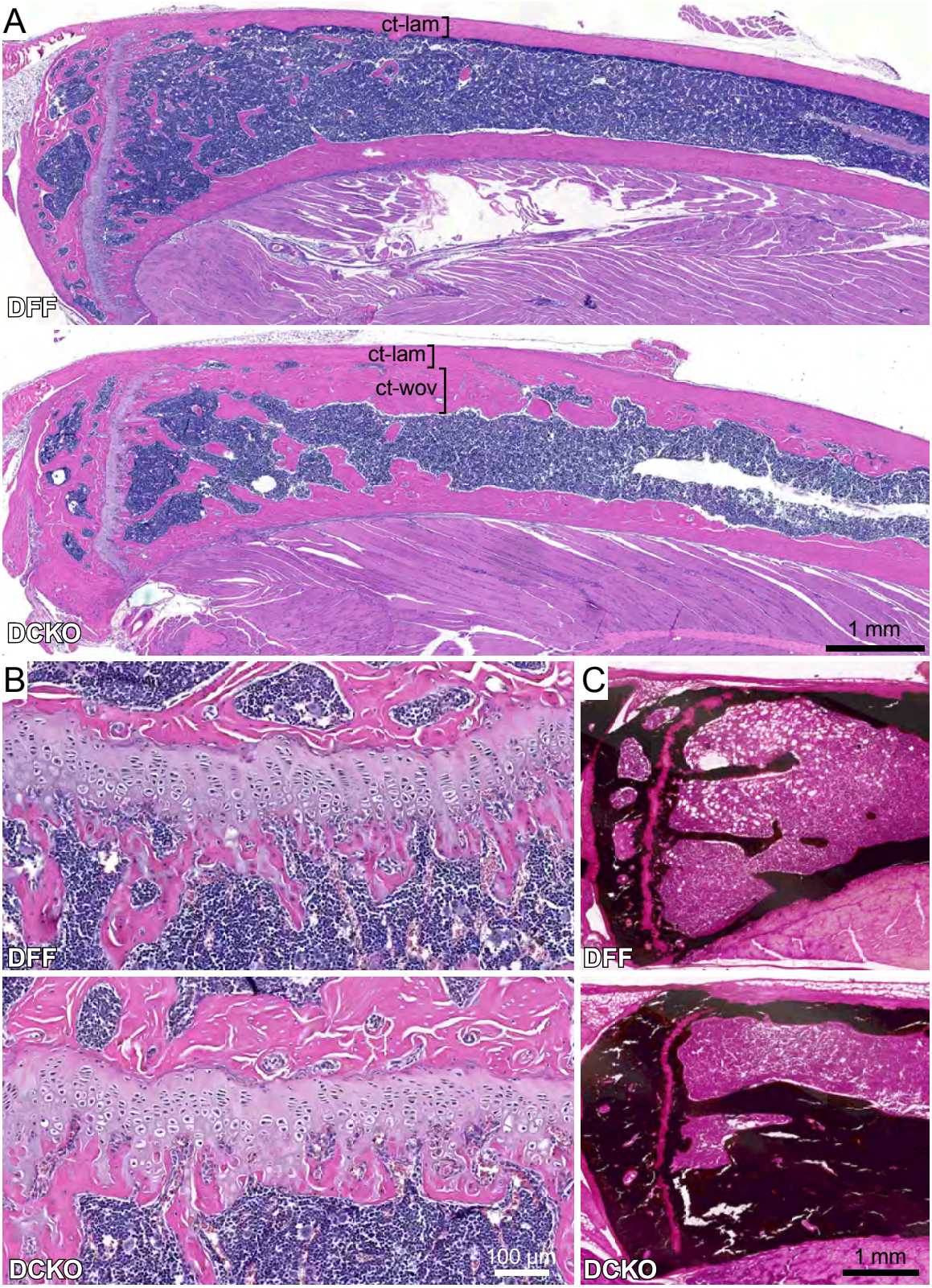
A
ct-lam
DFF
ct-lam
ct-wov
DCKO
1 mm
B
DFF
DCKO
100 µm
C
DFF
DCKO
1 mm

Figure 4

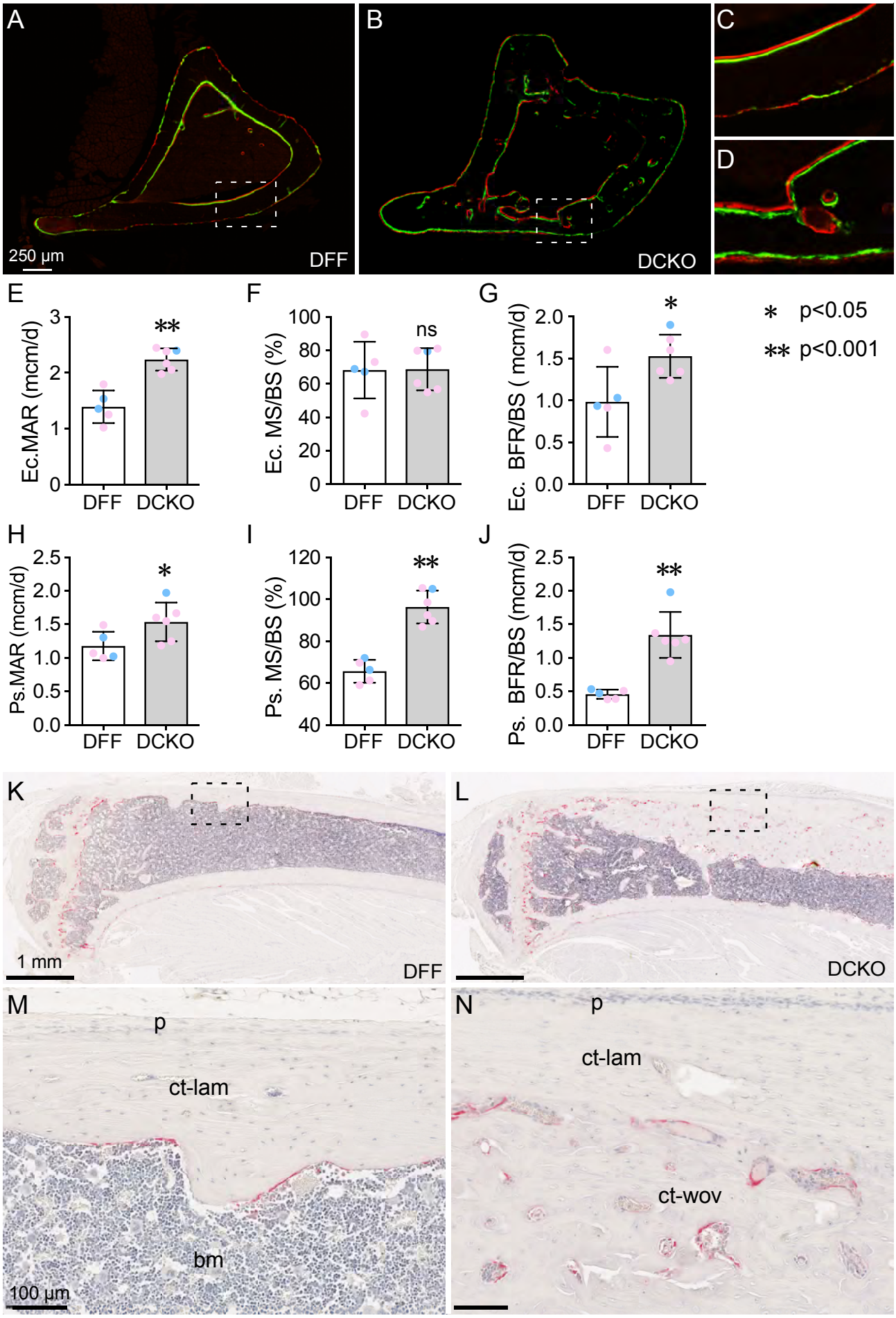
A
250 µm
DFF
B
DCKO
C
D
E
Ec.MAR (mcm/d)
**
DFF
DCKO
F
Ec. MS/BS (%)
ns
G
Ec. BFR/BS (mcm/d)
*
* p<0.05
** p<0.001
H
Ps.MAR (mcm/d)
I
Ps. MS/BS (%)
J
Ps. BFR/BS (mcm/d)
K
1 mm
L
M
p
ct-lam
bm
100 µm
N
ct-wov

Figure 5

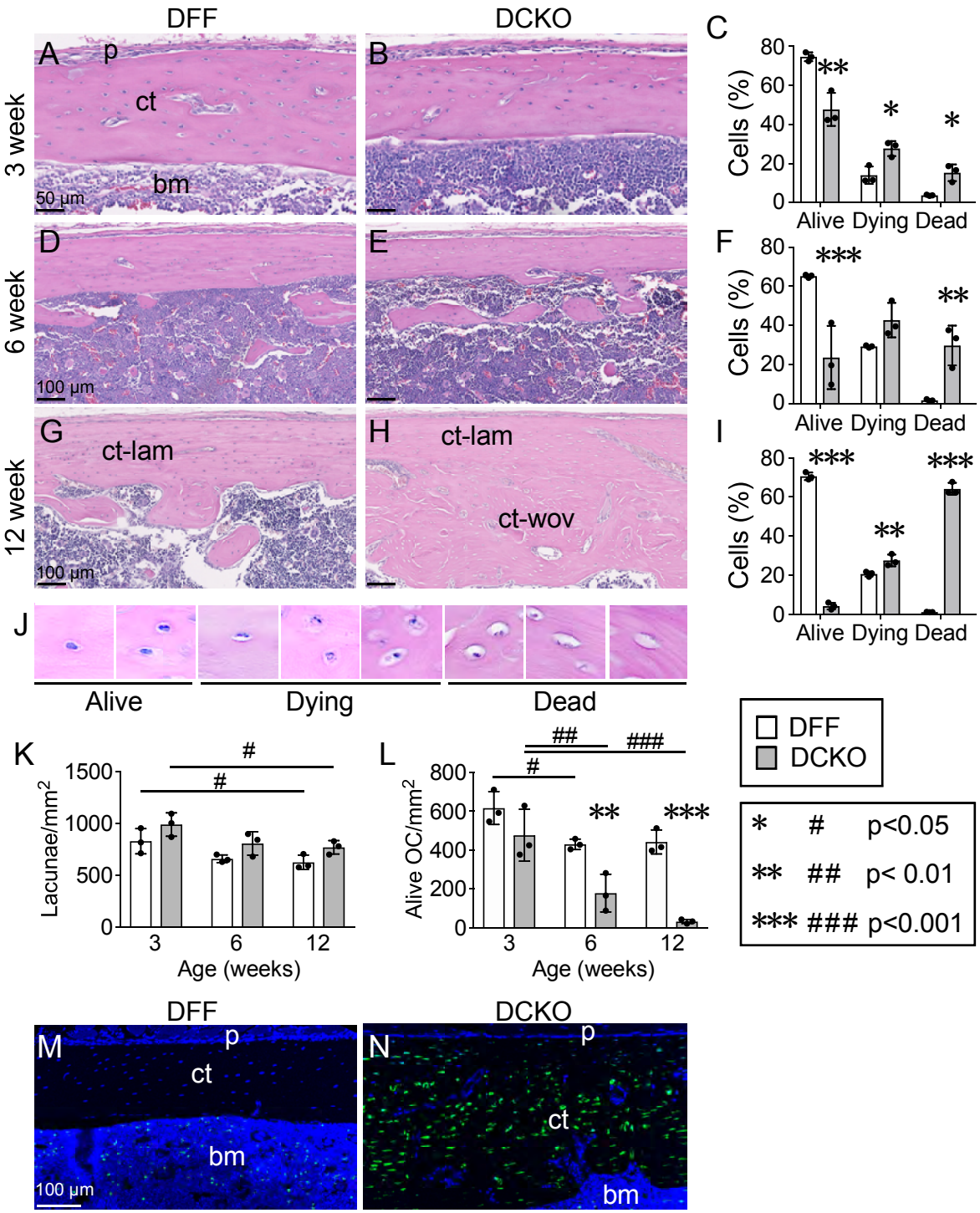
DFF
DCKO
3 week
6 week
12 week
A
B
C
D
E
F
G
H
I
J
K
L
M
N
p
ct
bm
ct-lam
ct-wov
50 µm
100 µm
Cells (%)
Alive
Dying
Dead
Lacunae/mm2
Alive OC/mm2
Age (weeks)
DFF
DCKO
* # p<0.05
** ## p< 0.01
*** ### p<0.001

Figure 6

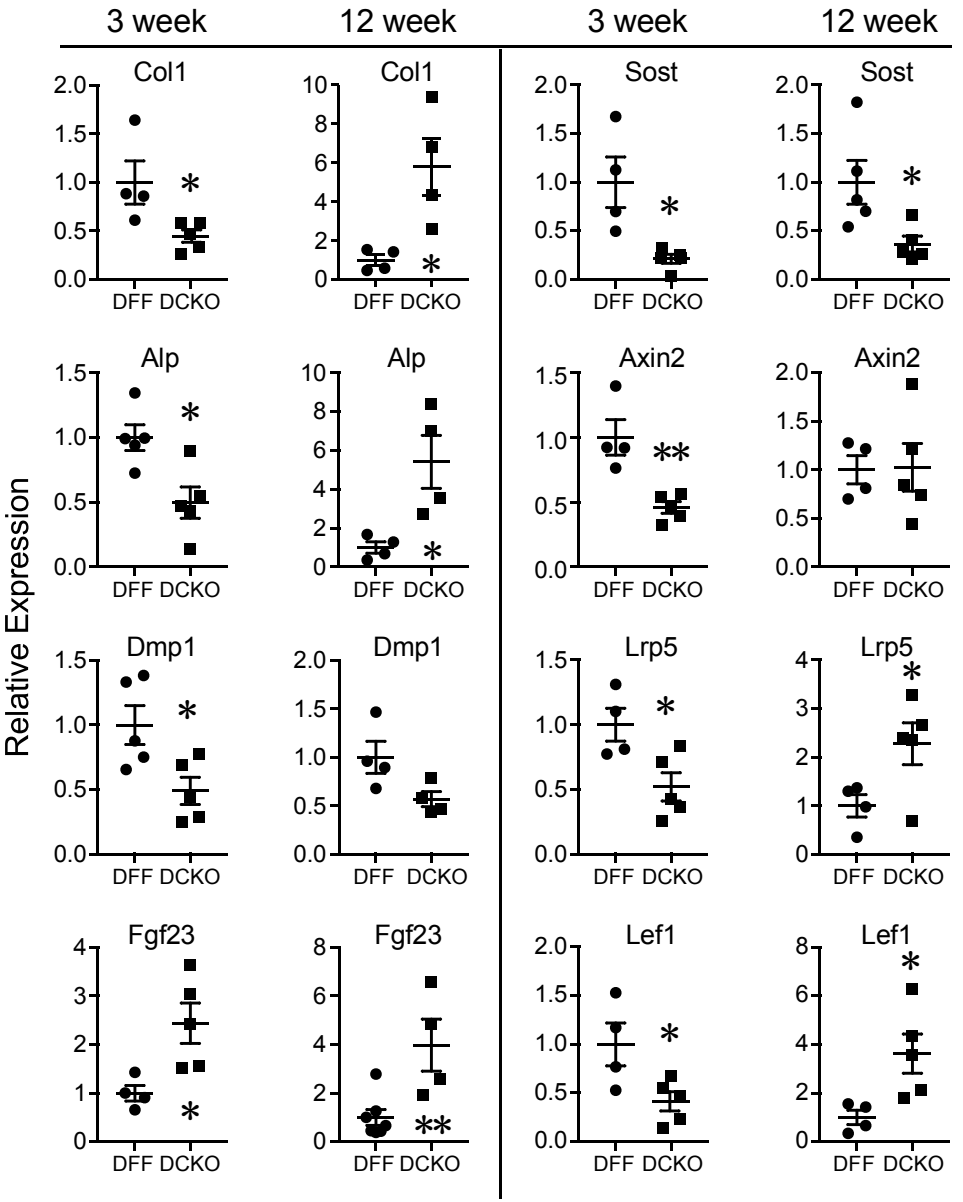
3 week
12 week
3 week
12 week
Relative Expression
Col1
Col1
Sost
Sost
Alp
Alp
Axin2
Axin2
Dmp1
Dmp1
Lrp5
Lrp5
Fgf23
Fgf23
Lef1
Lef1
DFF DCKO
* p<0.05 ** p<0.01

Figure 7

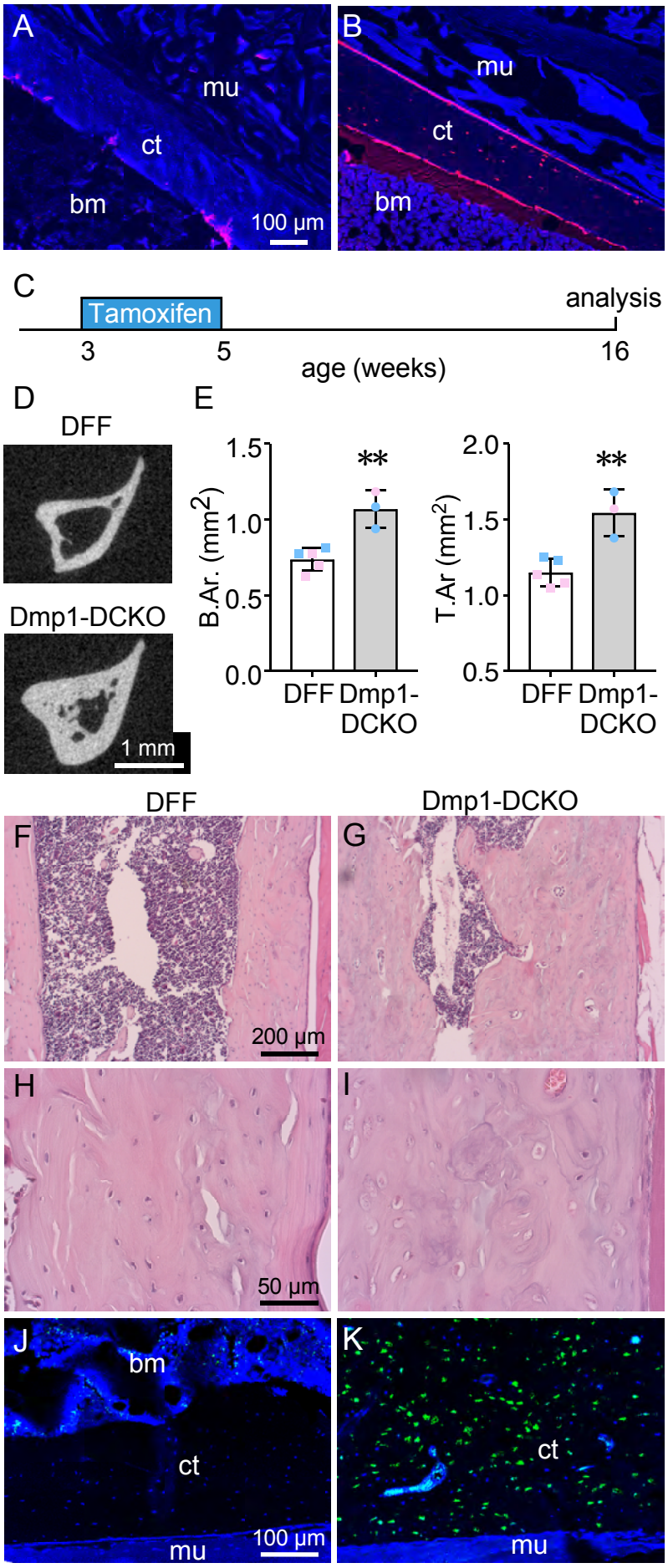
A
mu
ct
bm
100 µm
B
mu
ct
bm
C
Tamoxifen
analysis
3
5
16
age (weeks)
D
DFF
Dmp1-DCKO
1 mm
E
B.Ar. (mm2)
1.5
1.0
0.5
0.0
**
DFF
Dmp1-DCKO
T.Ar (mm2)
2.0
1.5
1.0
0.5
**
DFF
Dmp1-DCKO
DFF
Dmp1-DCKO
F
200 µm
G
H
50 µm
I
J
bm
ct
mu
100 µm
K
ct
mu

Supplemental Data

Supplemental Figure 1. Localization of the *OC-Cre* lineage and expression of *Fgfr1* and *Fgfr2* following conditional inactivation with *OC-Cre*. (A) *ROSA*^{mTmG} and *ROSA*^{Tomato} reporters. Recombination of the *ROSA*^{mTmG} allele exposed to *OC-Cre* activates membrane bound GFP (mG) in osteoblasts and osteocytes. Non-targeted cells express membrane bond Tomato (mT). Recombination of the *ROSA*^{Tomato} allele exposed to *OC-Cre* activates Tomato (red) in osteoblasts and osteocytes. Blue, DAPI; bm, bone marrow; ct, cortical bone. (B) Quantitative RT-PCR at 3 weeks of flushed cortical bone showing reduced expression of *Fgfr1* (3.5 fold) and *Fgfr2* (4.2 fold) in OC-*Fgfr1/2* DCKO mice compared to *Fgfr1/2* DFF control mice.

Supplemental Figure 2. Analysis of cortical bone in different allelic combinations of *Fgfr1* and *Fgfr2* targeted with *OC-Cre* demonstrating that increased bone mass only occurs when both copies of *Fgfr1* are deleted. (A) Quantitation of cortical area from mid tibial sections. (B) Quantitation of bone volume/total volume ratio (BV/TV) from proximal tibial sections. Statistics, 2-way ANOVA; group sample sized indicated by number within each bar.

Supplemental Figure 3. Expression of osteocyte markers, Sost and Dmp1, in cortical bone from 12-week-old OC-*Fgfr1/2* DCKO and *Fgfr1/2* DFF mice. bm, bone marrow; ct, cortical bone

Supplemental Table S1. MicroCT analysis of tibia and femur

	6 wk				12 wk			
	DFF		DCKO		DFF		DCKO	
	Mean	St.Dev.	Mean	St.Dev.	Mean	St.Dev.	Mean	St.Dev.
Tibia Cortical Bone								
T.Ar (mm^2)	1.45	0.20	1.73	0.07	1.22	0.17	2.15***	0.19
B.Ar (mm^2)	0.49	0.13	0.69	0.16	0.73	0.07	1.51***	0.13
Ct.Th (mm)	0.11	0.03	0.14	0.03	0.19	0.00	0.29	0.03
pMOI (mm^4)	0.21	0.07	0.34	0.09	0.26	0.06	0.61**	0.23
TMD ($mgHA/cm^3$)	895	44.7	878	37.3	1084	5.02	99***	15.1
Tibia Metaphyseal Bone								
TV (mm^3)	1.28	0.16	1.51	0.15	1.28	0.06	1.54	0.25
BV (mm^3)	0.46	0.15	0.65	0.21	0.50	0.06	0.83	0.19
BV/TV (mm^3/mm^3)	0.36	0.09	0.43	0.11	0.39	0.05	0.53	0.07
vBMD ($mgHA/cm^3$)	246	57.7	280	61.0	303	42.4	404	68.4
Femur Metaphyseal Bone								
TV (mm^3)	1.64	0.14	2.10***	0.18	1.59	0.07	2.23***	0.14
BV (mm^3)	0.59	0.20	0.83	0.32	0.59	0.05	1.14*	0.18
BV/TV (mm^3/mm^3)	0.35	0.10	0.39	0.13	0.37	0.04	0.51	0.05
vBMD ($mgHA/cm^3$)	246	64.1	266	86.5	304	26.1	385	46.3

	18 wk				24 wk				32 wk			
	DFF		DCKO		DFF		DCKO		DFF		DCKO	
	Mean	St.Dev.	Mean	St.Dev.	Mean	St.Dev.	Mean	St.Dev.	Mean	St.Dev.	Mean	St.Dev.
Tibia Cortical Bone												
T.Ar (mm^2)	1.17	0.17	2.39***	0.26	1.18	0.18	2.41***	0.37	1.29	0.17	2.47***	0.22
B.Ar (mm^2)	0.74	0.10	1.8***	0.23	0.78	0.10	1.95***	0.44	0.84	0.09	2.11***	0.48
Ct.Th (mm)	0.20	0.01	0.33**	0.05	0.21	0.01	0.38***	0.13	0.22	0.01	0.45***	0.10
pMOI (mm^4)	0.27	0.08	1.04***	0.21	0.28	0.09	1.17***	0.19	0.30	0.06	1.23***	0.26
TMD ($mgHA/cm^3$)	1122	14.3	1025***	27.8	1133	20.9	1059***	20.2	1185	19.2	1060***	20.7
Tibia Metaphyseal Bone												
TV (mm^3)	1.33	0.10	1.80**	0.28	1.39	0.24	1.86***	0.34	1.69	0.13	2.26*	0.28
BV (mm^3)	0.51	0.05	1.12***	0.30	0.57	0.17	1.38***	0.44	0.67	0.13	1.88***	0.22
BV/TV (mm^3/mm^3)	0.39	0.05	0.62**	0.14	0.41	0.07	0.73***	0.17	0.40	0.06	0.85***	0.17
vBMD ($mgHA/cm^3$)	343	57.6	539*	147	378	70.4	689***	208	417	88.8	878***	181.4
Femur Metaphyseal Bone												
TV (mm^3)	1.71	0.19	2.27***	0.22	1.74	0.18	2.31***	0.16	1.64	0.11	2.37***	0.25
BV (mm^3)	0.61	0.11	1.31***	0.33	0.64	0.14	1.53***	0.40	0.64	0.12	2.16***	0.14
BV/TV (mm^3/mm^3)	0.35	0.05	0.58**	0.13	0.37	0.07	0.67***	0.17	0.39	0.05	0.92***	0.05
vBMD ($mgHA/cm^3$)	312	37.6	493*	134	338	54.5	634***	204	386	28.1	948***	63.4

*p<0.05, **p<0.01, ***p<0.001 DCKO vs. DFF, Bonferroni's multiple comparisons

Supplemental Table S2. Biomechanics Analysis of femur at 24 wk

	DFF		DCKO	
	Mean	St.Dev.	Mean	St.Dev.
3-point bending				
Stiffness	120	41.9	175***	35.3
Maximum load	24.1	2.32	43.8***	2.76
post-yield displacement	0.192	0.122	0.056*	0.033
work-to fracture	6.28	1.92	7.44	2.10
yield load	21.3	2.62	40.1***	2.52
Young's modulus	5969	1884	1797***	413
Yield stress	174	29.9	98.0***	9.92
Maximum stress	196	19.3	107***	7.35
Moment of inertia	0.144	0.025	0.711***	0.107
RPI Testing				
First unloading slope (US 1st)	0.248	0.025	0.226	0.020
First indentation distance (ID 1st)	37.1	7.69	40.3	5.45
Total indentation distance (TID)	37.6	3.97	44.0	6.60
Initial indentation distance (IDI)	6.28	0.778	8.33	2.44
Cumulative indentation distance (CID)	1.13	0.137	1.42	0.540

*p<0.05, **p<0.01, ***p<0.001 DCKO vs. DFF unpaired t-test

Supplemental Figure 1

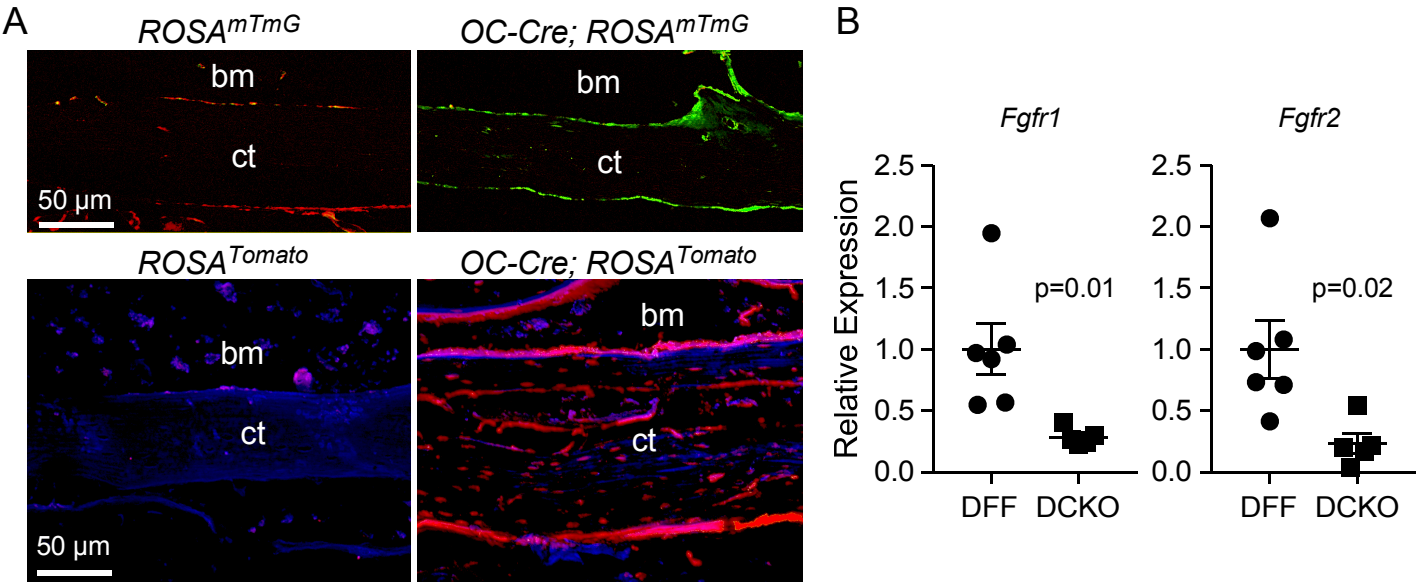

Supplemental Figure 2

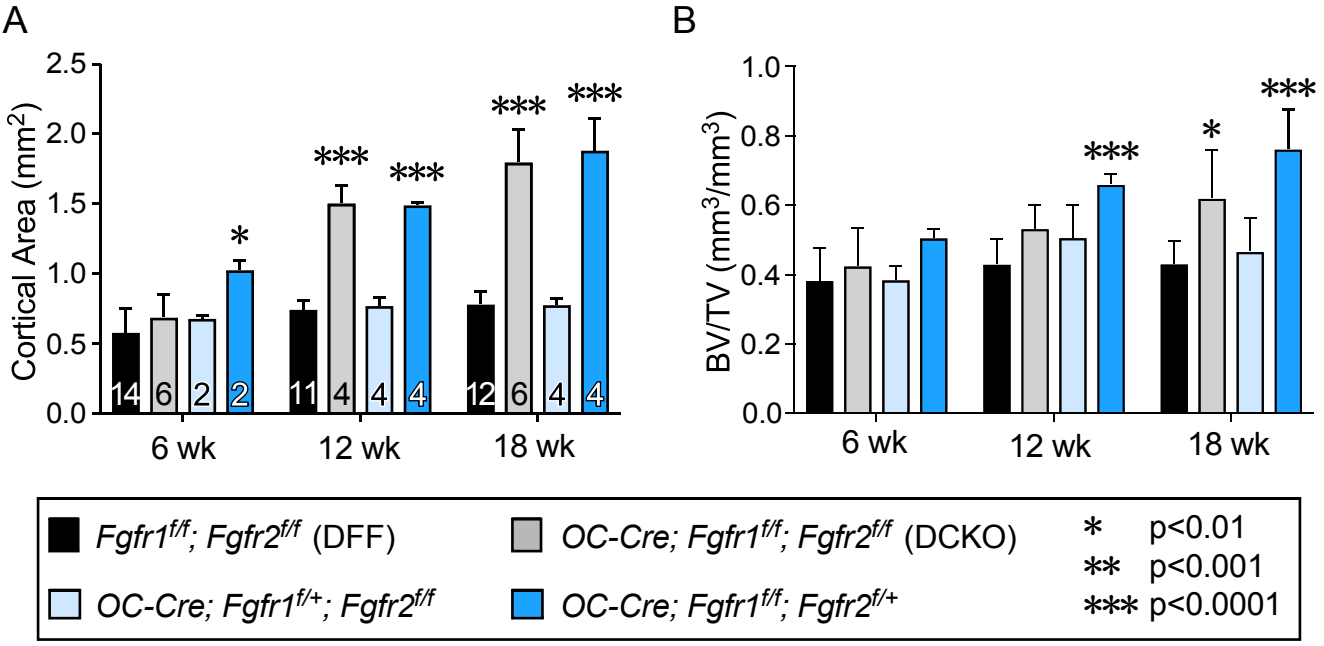
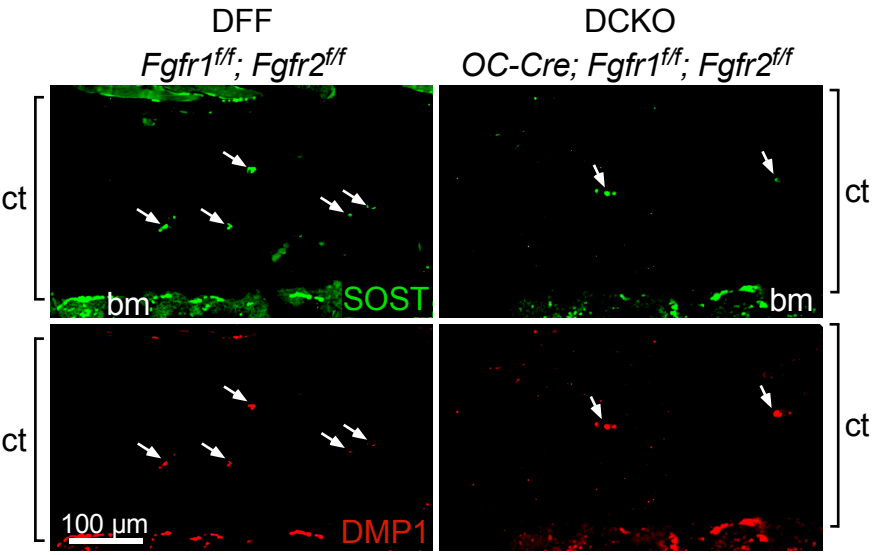
Supplemental Figure 3